



## Cite as

Nano-Micro Lett.  
(2025) 17:25Received: 21 May 2024  
Accepted: 28 August 2024  
© The Author(s) 2024

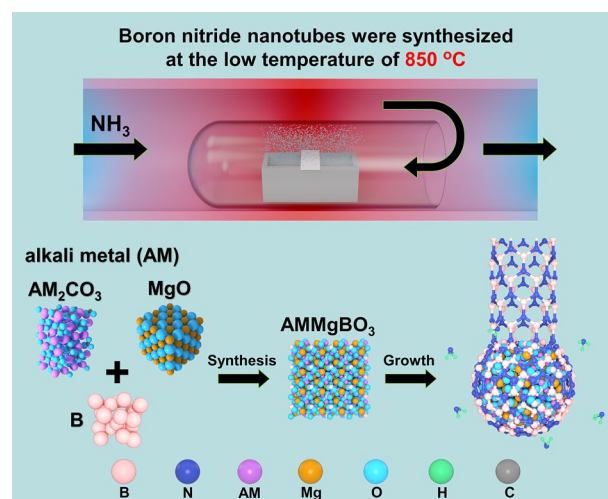
# An Efficient Boron Source Activation Strategy for the Low-Temperature Synthesis of Boron Nitride Nanotubes

Ying Wang<sup>1</sup>, Kai Zhang<sup>1</sup>, Liping Ding<sup>2</sup>, Liyun Wu<sup>1</sup>, Songfeng E<sup>3</sup>, Qian He<sup>1</sup>,  
Nanyang Wang<sup>1</sup>, Hui Zuo<sup>4</sup>, Zhengyang Zhou<sup>1</sup>, Feng Ding<sup>5</sup>, Yue Hu<sup>4</sup> ✉, Jin Zhang<sup>6</sup> ✉,  
Yagang Yao<sup>1</sup> ✉

## HIGHLIGHTS

- Developed more efficient boron activation strategies, while establishing various low-melting growth systems.
- The preparation temperature of boron nitride nanotubes has been reduced to 850 °C.

**ABSTRACT** Lowering the synthesis temperature of boron nitride nanotubes (BNNTs) is crucial for their development. The primary reason for adopting a high temperature is to enable the effective activation of high-melting-point solid boron. In this study, we developed a novel approach for efficiently activating boron by introducing alkali metal compounds into the conventional MgO–B system. This approach can be adopted to form various low-melting-point AM–Mg–B–O growth systems. These growth systems have improved catalytic capability and reactivity even under low-temperature conditions, facilitating the synthesis of BNNTs at temperatures as low as 850 °C. In addition, molecular dynamics simulations based on density functional theory theoretically demonstrate that the systems maintain a liquid state at low temperatures and interact with N atoms to form BN chains. These findings offer novel insights into the design of boron activation and are expected to facilitate research on the low-temperature synthesis of BNNTs.



**KEYWORDS** Boron nitride nanotubes; Low-temperature; Boron activation; Density functional theory

Ying Wang, Kai Zhang and Liping Ding have contributed equally to this work.

✉ Yue Hu, [yuehu@wzu.edu.cn](mailto:yuehu@wzu.edu.cn); Jin Zhang, [jinzhang@pku.edu.cn](mailto:jinzhang@pku.edu.cn); Yagang Yao, [ygyao2018@nju.edu.cn](mailto:ygyao2018@nju.edu.cn)

<sup>1</sup> National Laboratory of Solid State Microstructures, College of Engineering and Applied Sciences, Jiangsu Key Laboratory of Artificial Functional Materials, and Collaborative Innovation Center of Advanced Microstructures, Nanjing University, Nanjing 210093, People's Republic of China

<sup>2</sup> School of Electronic Information and Artificial Intelligence, Shaanxi University of Science & Technology, Xian 710000, People's Republic of China

<sup>3</sup> College of Bioresources Chemical and Materials Engineering, Shaanxi University of Science & Technology, Xian 710000, People's Republic of China

<sup>4</sup> Key Laboratory of Carbon Materials of Zhejiang Province, College of Chemistry and Materials Engineering, Wenzhou University, Wenzhou 325000, People's Republic of China

<sup>5</sup> Shenzhen Institutes of Advanced Technology, Chinese Academy of Sciences, Shenzhen 518000, People's Republic of China

<sup>6</sup> College of Chemical and Molecular Engineering, Peking University, Beijing 100871, People's Republic of China

Published online: 27 September 2024



SHANGHAI JIAO TONG UNIVERSITY PRESS

Springer

## 1 Introduction

Boron nitride nanotubes (BNNTs) [1–3] are one-dimensional tubular nanostructures with excellent physical and chemical properties. These properties include high mechanical strength [4], low weight [5], high temperature resistance [6, 7], strong interfacial bonding [8], and electrical insulation [9]. These properties make BNNTs highly promising for various applications, including thermal interface materials, high-temperature-resistant materials, radiation shielding materials, and deep ultraviolet emitters [10–13].

Nevertheless, the high cost of BNNTs has slowed the progress of research within the aforementioned fields. Lowering the synthesis temperature helps reduce costs because high synthesis temperatures (with the current synthesis temperature being 1100–8000 °C) increase instrument complexity and energy consumption [14–31]. To enhance the economic feasibility of BNNTs, it is imperative to thoroughly research their growth mechanisms, identify the factors that necessitate a high synthesis temperature, and thereby establish ways of lowering the synthesis temperature.

The synthesis of BNNTs typically follows the vapor–liquid–solid (VLS) growth mechanism. This process involves the dissolution and precipitation of boron and nitrogen sources in a liquid catalyst. The utilization of boron sources in growth systems has been limited primarily by the high toxicity of gaseous boron sources (i.e.,  $B_2H_6$ ,  $B_{10}H_{14}$ ,  $BCl_3$ ) and the extremely high melting point (2076 °C) of solid boron when compared with the wide use of gaseous nitrogen sources ( $N_2$ ,  $NH_3$ ). The conversion of solid B into a highly activated state demands much energy, which is a major contributing factor to the high growth temperature. Our primary task, therefore, is to explore a method of activating boron that is not only low energy but also efficient to reduce the growth temperature.

Over the years, methods of activating boron have been primarily categorized into physical and chemical techniques. Physical techniques include laser ablation [14, 15], thermal plasma [16, 17], and arc discharge [18, 19] methods. These methods use the high temperatures generated by lasers, plasma, and arc discharge to break down the boron, resulting in highly active boron atoms. These atoms then aggregate into boron droplets, which are used in BNNT synthesis. Despite their ability to produce high-quality BNNTs, physical methods have drawbacks, including the

requirement for complex and expensive equipment and extremely high reaction temperatures (3500–8000 °C) (Table S1). An alternative approach that combines physical and chemical techniques for boron activation is the adoption of the ball milling and annealing method [20–22]. Mechanical ball milling reduces the size of boron such that the boron reacts with  $NH_3$  to form activated B–N nanoparticles. These nanoparticles subsequently crystallize into nanotubular structures during annealing. Although this method lowers the required activation temperature to 1100–1300 °C, it has limitations, including a relatively low efficiency in activating boron and a susceptibility to the deactivation of active boron (Table S1).

In comparison, boron oxide chemical vapor deposition (BOCVD) [23–31] is a promising method for boron activation in the field of chemical technology. This method involves the reaction of metal oxides ( $MeO_x$ ) with boron at high temperatures, resulting in the formation of  $B_xO_y$  and metal vapor. Once the vapor pressure in the system reaches saturation, the  $B_xO_y$  and metal vapor interact and condense into highly activated Me–B–O liquid particles [32–35]. These liquid particles undergo supersaturation and precipitation of B–N chains in the presence of  $NH_3$ , resulting in the formation of BNNTs. The advantages of this method are its simple equipment, the controllability of the reaction, the high activation efficiency of the boron, and the high quality of the prepared BNNTs (Table S1).

However, the current growth temperature range (1100–1500 °C) of BOCVD is high due to the activity of the Me–B–O growth system formed. An analysis of phase diagrams reveals that compounds in the Me–B–O system containing highly catalytic metals (Me = Mg, Fe, Al, Ca) typically have high melting points, resulting in low catalytic growth activity of the system at lower temperatures (Fig. S1). The above analysis indicates the necessity of a more thorough investigation of the conventional MgO–B growth system (where a schematic diagram of the experiment is shown in Fig. S2) [36]. MgO has exceptional activation effects on B, effectively constructing the Mg–B–O growth system (where detailed experimental explanations are presented in Fig. S3). The high-melting-point compound  $Mg_2B_2O_5$  (1307 °C) [37] generated in this system has a strong catalytic capability for BNNT growth at high temperatures. However, this compound deviates from the VLS growth mechanism in that it does not liquefy at lower

temperatures, which hinders BNNT growth. Therefore, it is crucial to lower the melting point of the Mg–B–O system with high catalytic activity.

As is well known, alkali metals (AMs) such as Li, Na, K, Rb, and Cs have extremely high reactivity, which is highly beneficial for activating B. Furthermore, compounds formed in the AM–B–O system typically have lower melting points, which can keep the growth system in a liquid state at reduced temperatures (Fig. S4). Therefore, in this work, we designed a method of incorporating AM compounds into the conventional MgO–B growth system. The designed method was used to establish a variety of low-melting-point AM–Mg–B–O systems, enabling efficient BNNT synthesis at a mild temperature of 950 °C and even facilitating BNNT synthesis at temperatures as low as 850 °C. Incidentally, the lowest synthesis temperature in this study is already comparable to the synthesis temperature of non-growth methods (e.g., template methods) [38, 39]. In addition, molecular dynamics simulations based on density functional theory theoretically demonstrated that the systems maintain a liquid state at low temperatures and interact with N atoms to form BN chains. This paper thus provides an innovative method for designing lower-melting-point and high-activity systems in low-temperature environments, with noteworthy implications for future research on low-temperature BNNT synthesis. As an example application, an BNNT/epoxy resin (EP) composite film, comprising 5 wt% BNNTs, exhibits remarkable thermal dissipation capabilities.

## 2 Experimental Section

### 2.1 Materials

The horizontal resistance heating furnace (GSL–1500X) was provided by Hefei Cogent Materials Technology Co., Ltd. Argon and ammonia gases were supplied by Nanjing Tezhong Gas Factory Co., Ltd. Boron powder (B), magnesium oxide (MgO), and potassium carbonate ( $K_2CO_3$ ), lithium carbonate ( $Li_2CO_3$ ), sodium carbonate ( $Na_2CO_3$ ), rubidium carbonate ( $Rb_2CO_3$ ), cesium carbonate ( $Cs_2CO_3$ ), isopropanol ( $C_3H_8O$ ) and ethyl acetate ( $C_4H_8O_2$ ) were purchased from Shanghai Aladdin Biochemical Technology Co., Ltd. Epoxy resin (EP) was supplied by Shanghai Yuanye Biotechnology Co., Ltd.

### 2.2 Preparation of BNNTs

BNNTs were synthesized in a horizontal resistance heating furnace consisting of an alumina tube with a length of 60 cm and a diameter of 5 cm. The  $SiO_2/Si$  substrates and 200 mg of MgO,  $K_2CO_3$ , and B precursors (molar ratio 1:1:4) were placed on the top and inside of the BN boat, respectively. The boat was positioned near the closed-end of a 20 cm long, 3 cm diameter alumina tube. This small tube was placed inside a horizontal resistance heating furnace, and the closed-end was kept in the center of the heating zone (as shown in Fig. S2). The furnace was continuously supplied with 50 standard cubic centimeters per minute (sccm) Ar and heated to the growth temperature at a rate of 10 °C  $min^{-1}$ . Subsequently, the Ar was replaced with 50 sccm  $NH_3$  and maintained for 2 h to enable the growth of BNNTs. The resulting sample was then cooled to room temperature under Ar protection.

### 2.3 Preparation of BNNT/EP Composite Films

A homogeneous solution was formed by mixing 10 mL of isopropanol, 10 mL of ethyl acetate, and 2 g of EP at 60 °C and a stirring rate of 500  $r\ min^{-1}$ . Then, 0.1 g of BNNTs was added to the EP solution and kept under the same stirring and temperature conditions until the solution became a viscous and homogeneous mixture. A curing agent, diethylenetriamine, was then added to the mixture in a quantity of 200  $\mu L$ . After stirring for 2 min, the mixture was poured into a Teflon Petri dish and cured at 60 °C for 2 h to produce the composite film.

## 3 Results and Discussion

### 3.1 Growth Results of BNNTs in the K–Mg–B–O System

We initially present the growth outcomes of incorporating K, an AM, into MgO–B. Optical photographs and scanning electron microscopy (SEM) images of the growth results for MgO,  $K_2CO_3$ , and B with a molar ratio of 1:1:4 reveal the deposition of white products, including slender BNNTs, on  $SiO_2/Si$  substrates at growth temperatures of 1000 and 1100 °C (Fig. 1a, b). At a growth temperature of 900 °C, a minimal quantity of product was acquired on the  $SiO_2/Si$  substrate (Fig. 1c). Nonetheless, BNNT

synthesis was unsuccessful at 800 °C (Fig. 1d). X-ray diffraction (XRD) and Raman spectra analyses were conducted for the products on the SiO<sub>2</sub>/Si substrates obtained at growth temperatures of 900, 1000, and 1100 °C. The peaks observed in the XRD patterns correlate with distinctive signals of h-BN (JCPDS No. 73–2095), signifying that the as-grown samples have h-BN structures (Fig. 1e). The Raman spectra have a pronounced absorption band at 1368 cm<sup>-1</sup>, corresponding to the E<sub>2g</sub> in-plane vibration mode of h-BN (Fig. 1f). The XRD patterns suggest that the products within the BN boat encompass BN (JCPDS No. 73–2095), MgO (JCPDS No. 87–0652), and a minor quantity of B<sub>13</sub>C<sub>2</sub> (JCPDS No. 71–0108) (resulting from the reaction between CO<sub>2</sub> from K<sub>2</sub>CO<sub>3</sub> decomposition and B) (Fig. S5). This indicates that the system's

precursors undergo efficient transformation into BN even at low temperatures.

Furthermore, a more thorough temperature investigation revealed a temperature of 950 °C to be suitable for efficient growth. White material (BNNTs) was observed on the precursor material and along the inner walls of the BN boat, as illustrated in Fig. S6a. SEM images unveiled that these white products comprised an extensive region of densely packed filamentous BNNTs, having an estimated length of several micrometers to tens of micrometers (Figs. S6b and 1g). In addition, apart from XRD and Raman spectra affirming the h-BN structure of the samples cultivated at 950 °C (Fig. S6c, d), further characterization was undertaken via Fourier transform infrared spectroscopy and transmission electron microscopy (TEM) for a more comprehensive analysis. In Fig. 1i,

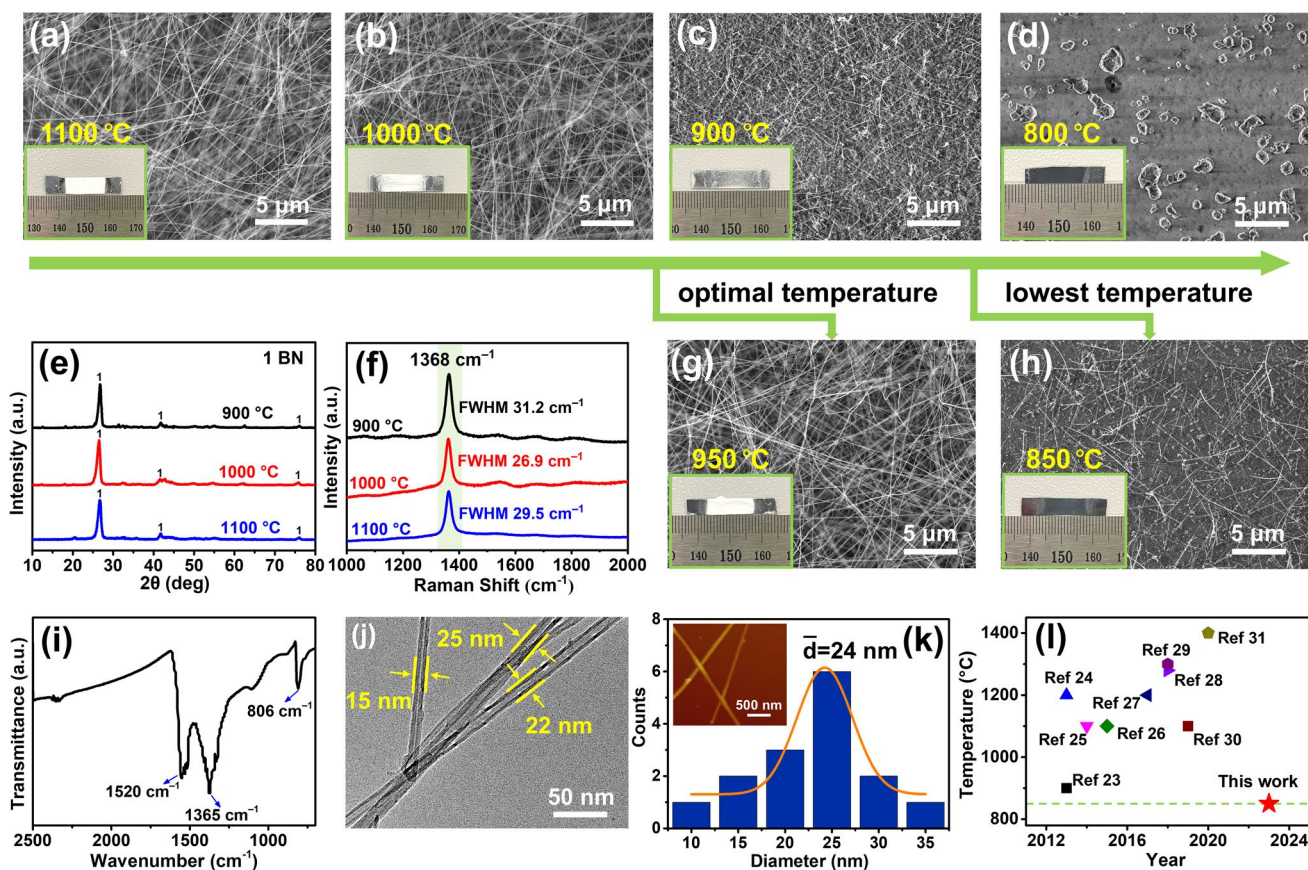


**Fig. 1** Fundamental characterization of BNNTs. SEM images of products grown on SiO<sub>2</sub>/Si substrates at **a** 1100 °C, **b** 1000 °C, **c** 900 °C, **d** 800 °C, **g** 950 °C, and **h** 850 °C. Inset: photograph of products formed on SiO<sub>2</sub>/Si substrates. **e** XRD patterns and **f** Raman spectra of products formed at 900, 1000, and 1100 °C. **i** Fourier transform infrared spectrum of products formed at 950 °C. **j** Low-magnification TEM images of the BNNTs. **k** Diameter distribution of the BNNTs (inset: typical AFM image of BNNTs dispersed on the SiO<sub>2</sub>/Si substrates). **l** Comparison of growth temperatures between previous reports and this work

there are three absorption bands at approximately 1520, 1365, and 806  $\text{cm}^{-1}$ . The absorption peak at 806  $\text{cm}^{-1}$  corresponds to a B–N–B bending vibration parallel to the *c*-axis whereas the absorption peak at 1365  $\text{cm}^{-1}$  corresponds to a B–N stretching vibration perpendicular to the *c*-axis. Both of these peaks are characteristic of BN. The absorption peak at 1520  $\text{cm}^{-1}$  is associated with the vibration of the BN skeleton along the tangential direction of the nanotubes, which is a distinct characteristic of BNNTs. The TEM images reveal that the samples have elongated and straight hollow tubular structures, with diameters ranging from 15 to 25 nm (Fig. 1j). The interplanar spacing of the wall, which is characteristic of a  $d_{(002)}$  spacing of h-BN, is approximately 0.34 nm (Fig. S6e). The BNNTs were then dispersed onto  $\text{SiO}_2/\text{Si}$  substrates to obtain diameter statistics. SEM images (Fig. S6f) and atomic force microscopy (AFM) images (Fig. 1k inset) depict the relatively isolated and well-dispersed nature of the BNNTs on a  $\text{SiO}_2/\text{Si}$  substrate. The primary diameter distribution of the BNNTs, spanning from 10 to 35 nm and averaging 24 nm, is illustrated in Fig. 1k. All of the above results substantiate the effective synthesis of high-quality BNNTs at a modest temperature of 950 °C. Finally, and most surprisingly, the system accomplished BNNT synthesis at a minimum temperature of 850 °C (Fig. 1h). A comparison of the lowest growth temperature (850 °C) in this study with previously reported temperatures (Fig. 1l) reveals the achievement of this study (refer to Table S2 for detailed information).

### 3.2 Analysis of the Reasons for Low-Temperature Synthesis in the K-Mg-B-O System

Subsequently, the growth mechanism of the system was investigated. The initial stage comprised annealing  $\text{MgO}$ ,  $\text{K}_2\text{CO}_3$ , and B under Ar at 850 °C to investigate the authentic active constituents of the precursors during the growth process. The XRD pattern indicates that the product that formed after annealing the precursors was  $\text{KMgBO}_3$  (ICSD No. 174336) (Fig. S10a) (Fig. 2a) [40, 41]. The melting point of this compound was then investigated adopting differential scanning calorimetry (DSC). Figure 2b shows a clear endothermic peak at 825 °C, corresponding to the melting point of  $\text{KMgBO}_3$ . We consider that this compound has a reduced melting point, rendering it a pivotal determinant for

BNNT growth at reduced temperatures. For theoretical support, density-functional-theory-based molecular dynamics (DFT-MD) simulations were conducted to study the melting of  $\text{KMgBO}_3$  and the mechanism of BNNT growth from liquid  $\text{KMgBO}_3$  via a VLS mechanism at low temperature. The root mean square deviation (RMSD) can be used as an indicator of the dissolution of alloys [42–44] and clusters [45, 46]. We first ran DFT-MD simulations to test the states of a  $\text{KMgBO}_3$  slab at different temperatures and calculated the RMSD (Fig. 2c). Snapshots of MD simulations taken at 10 ps (Fig. S7) clearly show that the  $\text{KMgBO}_3$  slab melted at ~1100 K, which is in good agreement with the DSC data and the lowest temperature for BNNT growth, namely ~850 °C. To further simulate the growth of BNNT catalyzed by  $\text{KMgBO}_3$ , MD simulations were performed at 1100 K for a total duration of 20 ps, with a time step of 1 fs. By adding N atoms to the surface of liquid  $\text{KMgBO}_3$ , we found that N atoms were intercalated into the B–O bonds of  $\text{BO}_3^{3-}$ . Snapshots of the MD trajectory are presented in Fig. 2d and Movie S1. The intercalation of N atoms led to the formation of N–B pairs (red circles in Fig. 2d), N–B–N trimers (black circles), and N–B–N–N–B (green circles) short chains at 1100 K, suggesting that liquified  $\text{KMgBO}_3$  promoted the formation of h-BN on its surface. Remarkably, these B–N chains remained intact throughout the dynamics simulation (Movie S1), indicating that the B–N bonds were more favorable than the B–O bonds. Although we could not simulate the formation of a BNNT due to the huge computational costs of the DFT-MD simulations, these results clearly show that the nucleation of BN chains on the  $\text{KMgBO}_3$  surface is preferred and that the speculated VLS mechanism [47] of BNNT growth is thus reasonable. This finding has been confirmed by other studies [48–50]. To acquire conclusive proof of the catalytic role of  $\text{KMgBO}_3$  in BNNT growth, TEM characterization was performed for the BNNT tips. Figure 2e, f clearly shows that the catalytic particle resides at the tip's central point, encircled by layers of BN. This indicates that the BNNT grows from the catalyst particles, which is consistent with the VLS mechanism. Energy-dispersive X-ray spectroscopy (EDX) was adopted to investigate the BNNT tips. Elemental maps disclose the uniform distribution of B and N across the tip, with O and Mg being concentrated at the catalyst (Fig. 2g). In addition, the presence of K elements at the tip confirms that K has dissolved into the MgO–B system.



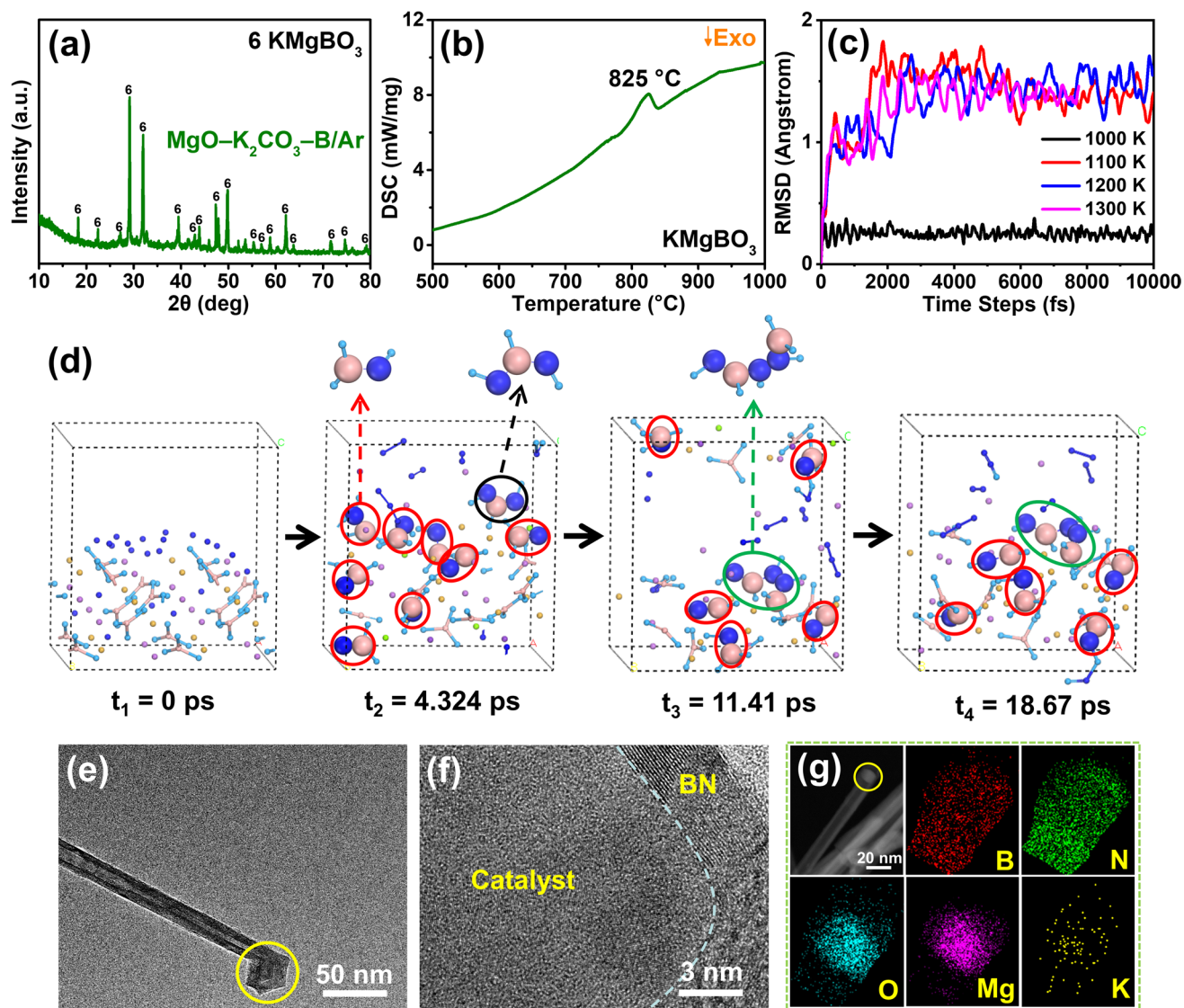


**Fig. 2** Experimental and theoretical analysis of the growth mechanism. **a** XRD patterns of products formed from MgO-K<sub>2</sub>CO<sub>3</sub>-B under Ar at 850 °C. **b** DSC curves of KMgBO<sub>3</sub>. **c** RMSD of the atoms of KMgBO<sub>3</sub> in MD simulations at different temperatures. **d** Formation of h-BN on the surface of KMgBO<sub>3</sub> observed in the MD simulation at 1100 K. Yellow: Mg, Purple: K, Light blue: O, Pink: B, Dark blue: N. **e** Low- and **f** high-magnification and **g** energy-dispersive X-ray spectroscopy mapping of the tip of the as-grown BNNTs

### 3.3 Growth Results of the K-B-O System and the AM-B-Mg-O System

To investigate whether the K-B-O system catalyzes the formation of nanotubes, we studied the activation effect of K<sub>2</sub>CO<sub>3</sub> on B at different temperatures and the growth results of K<sub>2</sub>CO<sub>3</sub> and B (with a molar ratio of 1:2 for K<sub>2</sub>CO<sub>3</sub> and B). The results reveal that a considerable quantity of white product formed on the SiO<sub>2</sub>/Si substrate at growth temperatures of 900, 1000, and 1100 °C. SEM images show that

the products obtained at all three temperatures had a flake-like structure inherent to BN (Fig. S8a-c). Furthermore, the XRD pattern of the products within the BN boat demonstrated a precursor reaction with NH<sub>3</sub>, yielding h-BN and a minor portion of B<sub>13</sub>C<sub>2</sub> (JCPDS No. 71-0108) (Fig. S8d). Subsequently, K<sub>2</sub>CO<sub>3</sub> and B were subjected to annealing at 950 °C to investigate their growth mechanism. The XRD pattern in Fig. S8e indicates the precursor's conversion into K<sub>2</sub>B<sub>4</sub>O<sub>7</sub> (JCPDS No. 70-1494), having a melting point of 780 °C [51]. We propose that in this growth process, the

elevated oxygen transfer propensity of  $K_2O$  (as per the Ellingham diagram) [52] enhances B activation, resulting in the creation of low-melting-point  $K_2B_4O_7$ . However, the pronounced reactivity of K renders it incapable of stable existence within the system, precluding its role in nucleation catalysis. This leads to a direct reaction between  $B_xO_y$  within  $K_2B_4O_7$  and  $NH_3$ , yielding BN nanosheets [35].

To investigate the effects of other AMs on the system, experiments were conducted by adding  $Li_2CO_3$ ,  $Na_2CO_3$ ,  $Rb_2CO_3$ , and  $Cs_2CO_3$  separately to the MgO–B system (MgO:AM $_2CO_3$ :B with a molar ratio of 1:1:4). SEM images show that all systems with Li, Na, Rb, and Cs grew extensive BNNTs at 950 °C (Fig. S9), and all four systems grew BNNT at a lower temperature of 850 °C (Fig. 3a–d). Subsequently, we annealed the four precursors in an Ar environment. XRD patterns revealed that, following annealing at 850 °C, the four precursors produced  $LiMgBO_3$  (JCPDS No. 79–1996) (Fig. S10b) [53],  $NaMgBO_3$  (ICSD No. 249567) (Fig. S10c) [54],  $RbMgBO_3$  (Fig. S10d) [55], and  $CsMgBO_3$  (Fig. S10e) [55] (Fig. 3e). We conducted DSC tests on these four products. Figure 3f shows that the melting points of  $LiMgBO_3$ ,  $NaMgBO_3$ ,  $RbMgBO_3$ , and  $CsMgBO_3$  are 785, 761, 860, and 774 °C, respectively.

and 774 °C, respectively. These results clearly indicate that AM readily dissolves into MgO–B, creating low-melting-point and highly catalytic AM–Mg–B–O systems and thus facilitating the low-temperature synthesis of BNNTs.

### 3.4 Exploration of BNNT Properties and Applications

We next explored the characteristics of the synthesized BNNTs. Thermogravimetric analysis indicates that carbon nanotubes (CNTs, Shanghai Aladdin Bio-Chem Technology Co., Ltd.) underwent oxidation at 500 °C, whereas the weight of BNNTs varied minimally within the temperature range of 25 to 1000 °C, signifying thermal stability superior to that of CNTs (Fig. S11a). We adopted the drop-casting method to measure the water contact angle (CA) of the BNNTs grown on the  $SiO_2/Si$  substrate. As is well-known, the CA is defined as the angle between the tangent to the gas–liquid interface at the triple point of gas, liquid, and solid phases and the solid–liquid boundary line on the liquid side. The size of the CA represents the degree of wettability. When the CA is 0°, it indicates complete wetting. When the CA is less than 90°, it indicates partial wetting or wetting. When the CA is greater than 90°, it

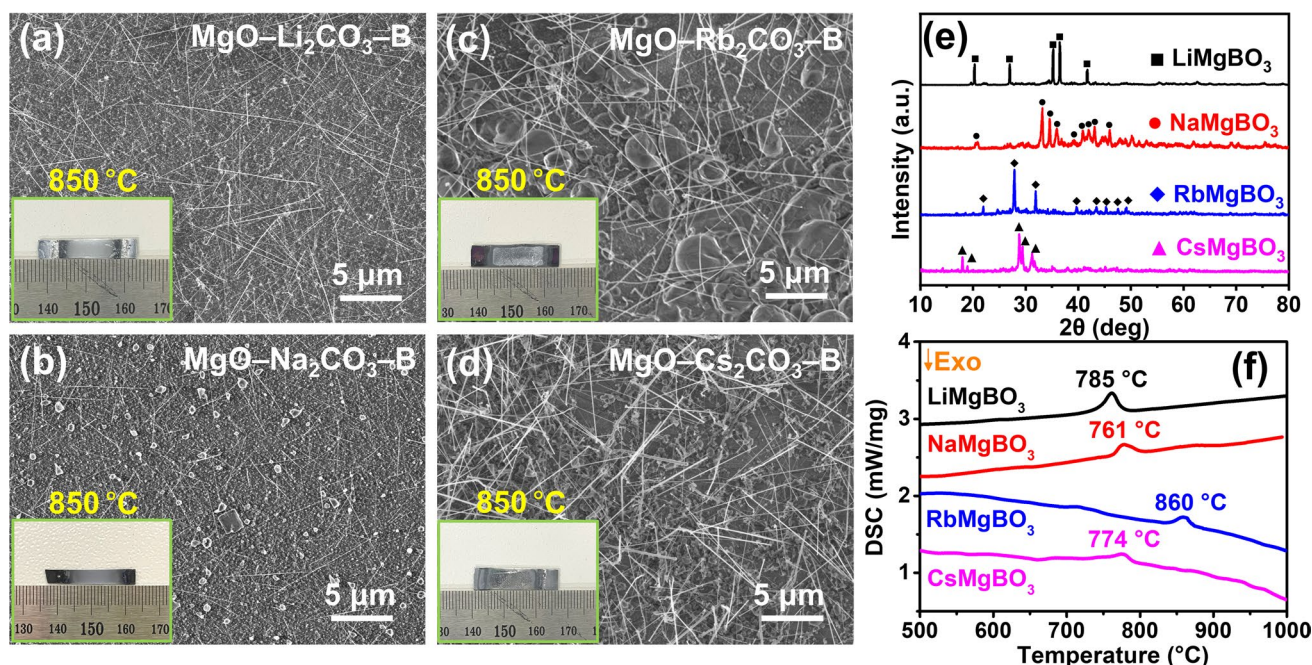


**Fig. 3** Various AMs used to grow BNNTs. SEM images of BNNTs grown on  $SiO_2/Si$  substrates from **a** MgO– $Li_2CO_3$ –B, **b** MgO– $Na_2CO_3$ –B, **c** MgO– $Rb_2CO_3$ –B, and **d** MgO– $Cs_2CO_3$ –B at 850 °C. **e** XRD patterns of products formed from MgO– $Li_2CO_3$ –B, MgO– $Na_2CO_3$ –B, MgO– $Rb_2CO_3$ –B, and MgO– $Cs_2CO_3$ –B under Ar at 850 °C. **f** DSC curves of  $LiMgBO_3$ ,  $NaMgBO_3$ ,  $RbMgBO_3$ , and  $CsMgBO_3$

indicates non-wetting. After a water droplet made contact with the SiO<sub>2</sub>/Si substrate, CA measurements were collected every 1 s for 10 s. The average CA was calculated as approximately 142.74°, indicating the stable hydrophobic nature of the BNNTs (Fig. 4a). Moreover, the BNNTs had consistent hydrophobic characteristics across a broad pH range spanning from 2 to 14 (Fig. S11b). These findings imply that the non-wettability of BNNTs remains impervious to potent acidic and alkaline conditions, making BNNTs highly promising for water-resistant coatings. An ultraviolet test was conducted on a suspension of BNNTs in ethanol. Figure 4b shows an absorption peak at approximately 5.9 eV (~210 nm), which is associated with the optical band gap of BNNTs and implies potential utility in ultraviolet-range photovoltaic devices. To examine the electrical traits of the samples, a single-BNNT-based device, featuring Cr (10 nm)/Au (80 nm) electrodes, was fabricated adopting electron beam lithography (Fig. 4c). A typical drain–source current versus drain–source voltage ( $I_{DS}$ – $V_{DS}$ ) curve of a single BNNT showed a current of  $7 \times 10^{-12}$  A and a resistance of  $1.4 \times 10^{11} \Omega$  at  $V_{DS} = 1$  V,

demonstrating the BNNT's good insulating property at room temperature due to the wide energy band gap of the nanomaterials (Fig. 4d).

The unique combination of high thermal conductivity and aspect ratio makes the BNNT an excellent filler for thermally conductive composites. A colorless and transparent pure EP film and white BNNT/EP composite film containing 5 wt% BNNT were separately fabricated using a solution method (Fig. 4e inset). SEM was conducted to characterize the fracture surface morphology of the composite materials. Figure S12 shows the uniform dispersion of interconnecting BNNTs throughout the composite. The XRD pattern of the pure EP film had wide diffraction peak dispersion between 15 and 23° [56], whereas the BNNT/EP composite film had a sharp peak at 26.8° corresponding to the (002) plane of h-BN (JCPDS No. 73–2095) in addition to the characteristic peaks of pure EP film (Fig. S13). The thermal conductivity of the sample was determined using the laser flash method. Figure 4e shows that the thermal conductivity of the 5 wt% BNNT/EP composite film increased to nearly  $1.87 \text{ W m}^{-1} \text{ K}^{-1}$  (in plane) and  $0.231 \text{ W m}^{-1} \text{ K}^{-1}$  (out of

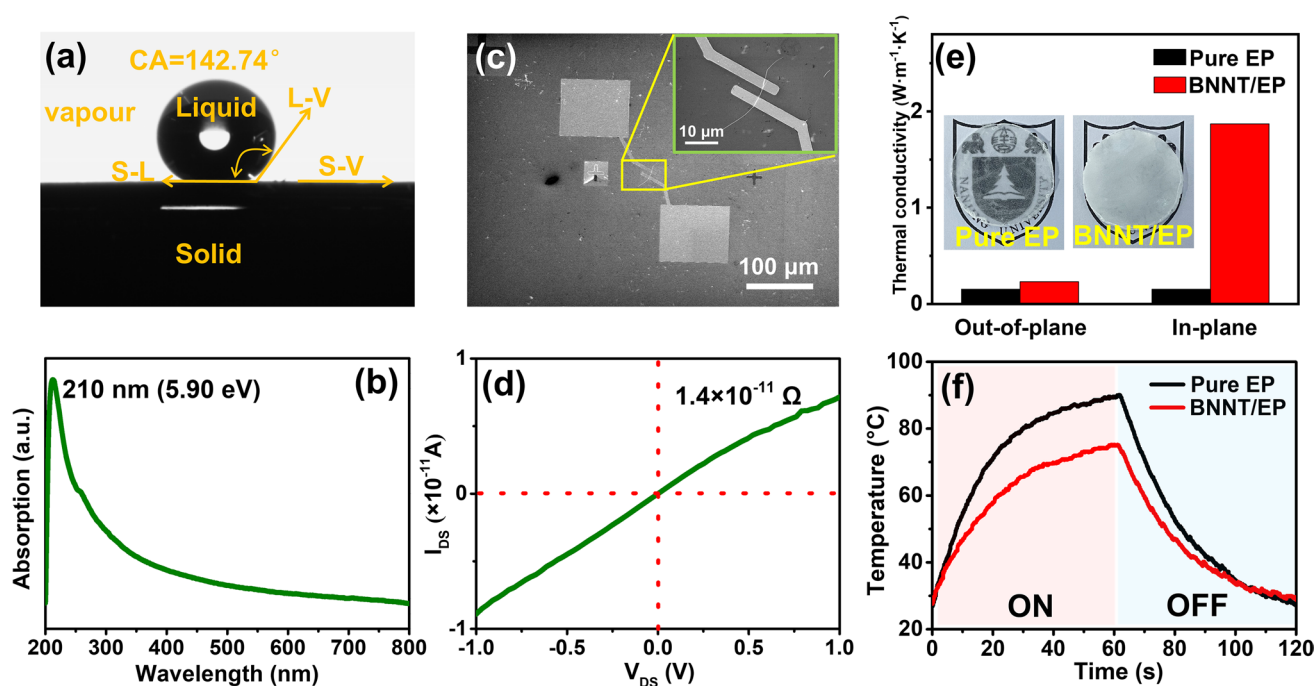


**Fig. 4** Properties and Applications of BNNTs. **a** Photographs of a CA measurement and **b** ultraviolet–visible absorption spectrum of as-grown BNNT-coated SiO<sub>2</sub>/Si. **c** SEM image and **d** typical  $I_{DS}$ – $V_{DS}$  curve of a single BNNT-based device. **e** In-plane and out-of-plane thermal conductivity. Inset: photograph of pure EP film and BNNT/EP composite film. **f** Surface temperature evolution over time of the pure EP film and BNNT/EP composite film



plane), approximately 12.2 times and 1.5 times higher than the values for the pure EP film, respectively. The BNNT/EP composite film was used as a thermal interface material for light-emitting diode (LED) chip heat dissipation, and the surface temperature changes of the LED chip were directly observed using an infrared thermal imager. Figures 4f and S14, respectively, show the variation of the core temperature of the LED chip with the running time and an infrared thermal image. During the 60 s that the LED chip was turned on, the center temperature of the BNNT/EP composite film was consistently 10–15 °C lower than that of the pure EP film. After turning off the LED chip, the core temperature of the BNNT/EP composite film dropped to 47.7 °C within 20 s, demonstrating the excellent heat dissipation ability of the BNNT/EP composite film. These findings demonstrate the application potential of BNNTs in thermal management.

## 4 Conclusions

In summary, we developed an effective strategy for activating boron by introducing AM compounds into the traditional MgO–B system. We thus formed several innovative AM–Mg–B–O systems with low melting points and strong catalytic capabilities. All of the AM systems synthesized BNNTs at a low temperature of 850 °C. MD simulations indicated that the representative compound  $\text{KMgBO}_3$  can liquefy at ~1100 K and react with N to produce BN chains. This outcome theoretically demonstrates the practicality of the systems for the synthesis of BNNTs at low temperatures. We believe that this work has implications for future research on the low-temperature synthesis of BNNTs. In addition, we prepared BNNT/EP composite films having a thermal conductivity 12.2 times that of pure EP films and excellent heat dissipation performance.

**Acknowledgements** This work was supported by the National Natural Science Foundation of China (No. 51972162) and the Fundamental Research Funds for the Central Universities (No. 2024300440).

**Author contributions** Ying Wang: Investigation, data curation, figure design, original draft writing, conceptualization. Kai Zhang: Data curation, figure design, conceptualization. Liping Ding: Theoretical calculation, conceptualization. Liyun Wu: Figure design. Songfeng E: Conceptualization. Qian He: Conceptualization. Nanyang Wang: Conceptualization. Hui Zuo: Data curation. Zhengyang Zhou: Data curation. Feng Ding: Theoretical calculation,

conceptualization. Yue Hu: Conceptualization, review and editing. Jin Zhang: Conceptualization, review and editing. Yagang Yao: Figure design, conceptualization, validation, original draft writing, review and editing, supervision.

## Declarations

**Conflict of interest** The authors declare no interest conflict. They have no known competing financial interests or personal relationships that could have appeared to influence the work reported in this paper.

**Open Access** This article is licensed under a Creative Commons Attribution 4.0 International License, which permits use, sharing, adaptation, distribution and reproduction in any medium or format, as long as you give appropriate credit to the original author(s) and the source, provide a link to the Creative Commons licence, and indicate if changes were made. The images or other third party material in this article are included in the article's Creative Commons licence, unless indicated otherwise in a credit line to the material. If material is not included in the article's Creative Commons licence and your intended use is not permitted by statutory regulation or exceeds the permitted use, you will need to obtain permission directly from the copyright holder. To view a copy of this licence, visit <http://creativecommons.org/licenses/by/4.0/>.

**Supplementary Information** The online version contains supplementary material available at <https://doi.org/10.1007/s40820-024-01521-2>.

## References

1. A. Rubio, J.L. Corkill, M.L. Cohen, Theory of graphitic boron nitride nanotubes. *Phys. Rev. B Condens. Matter* **49**, 5081–5084 (1994). <https://doi.org/10.1103/physrevb.49.5081>
2. X. Blase, A. Rubio, S.G. Louie, M.L. Cohen, Stability and band gap constancy of boron nitride nanotubes. *Europhys. Lett.* **28**, 335–340 (1994). <https://doi.org/10.1209/0295-5075/28/5/007>
3. N.G. Chopra, R.J. Luyken, K. Cherrey, V.H. Crespi, M.L. Cohen et al., Boron nitride nanotubes. *Science* **269**, 966–967 (1995). <https://doi.org/10.1126/science.269.5226.966>
4. N.G. Chopra, A. Zettl, Measurement of the elastic modulus of a multi-wall boron nitride nanotube. *Solid State Commun.* **105**, 297–300 (1998). [https://doi.org/10.1016/S0038-1098\(97\)10125-9](https://doi.org/10.1016/S0038-1098(97)10125-9)
5. X. Wei, M.-S. Wang, Y. Bando, D. Golberg, Tensile tests on individual multi-walled boron nitride nanotubes. *Adv. Mater.* **22**, 4895–4899 (2010). <https://doi.org/10.1002/adma.201001829>
6. Y. Chen, J. Zou, S.J. Campbell, G. Le Caer, Boron nitride nanotubes: pronounced resistance to oxidation. *Appl. Phys. Lett.* **84**, 2430–2432 (2004). <https://doi.org/10.1063/1.1667278>



7. L.H. Li, J. Cervenka, K. Watanabe, T. Taniguchi, Y. Chen, Strong oxidation resistance of atomically thin boron nitride nanosheets. *ACS Nano* **8**, 1457–1462 (2014). <https://doi.org/10.1021/nn500059s>
8. X.M. Chen, L.Y. Zhang, C. Park, C.C. Fay, X.Q. Wang et al., Mechanical strength of boron nitride nanotube-polymer interfaces. *Appl. Phys. Lett.* **107**, 253105 (2015). <https://doi.org/10.1063/1.4936755>
9. C. Harrison, S. Weaver, C. Bertelsen, E. Burgett, N. Hertel et al., Polyethylene/boron nitride composites for space radiation shielding. *J. Appl. Polym. Sci.* **109**, 2529–2538 (2008). <https://doi.org/10.1002/app.27949>
10. C.Y. Zhi, Y. Bando, C.C. Tang, Q. Huang, D. Golberg, Boron nitride nanotubes: functionalization and composites. *J. Mater. Chem.* **18**, 3900 (2008). <https://doi.org/10.1039/b804575e>
11. C. Zhi, Y. Bando, C. Tang, H. Kuwahara, D. Golberg, Grafting boron nitride nanotubes: from polymers to amorphous and graphitic carbon. *J. Phys. Chem. C* **111**, 1230–1233 (2007). <https://doi.org/10.1021/jp066052d>
12. X. Li, C. Zhi, N. Hanagata, M. Yamaguchi, Y. Bando et al., Boron nitride nanotubes functionalized with mesoporous silica for intracellular delivery of chemotherapy drugs. *Chem. Commun.* **49**, 7337–7339 (2013). <https://doi.org/10.1039/c3cc42743a>
13. Z.G. Chen, J. Zou, Q. Liu, C. Sun, G. Liu et al., Self-assembly and cathodoluminescence of microbelts from Cu-doped boron nitride nanotubes. *ACS Nano* **2**, 1523–1532 (2008). <https://doi.org/10.1021/nn800211z>
14. D. Golberg, Y. Bando, M. Eremets, K. Takemura, K. Kurashima et al., Nanotubes in boron nitride laser heated at high pressure. *Appl. Phys. Lett.* **69**, 2045–2047 (1996). <https://doi.org/10.1063/1.116874>
15. M.W. Smith, K.C. Jordan, C. Park, J.-W. Kim, P.T. Lillehei et al., Very long single- and few-walled boron nitride nanotubes via the pressurized vapor/condenser method. *Nanotechnology* **20**, 505604 (2009). <https://doi.org/10.1088/0957-4484/20/50/505604>
16. K.S. Kim, C.T. Kingston, A. Hrdina, M.B. Jakubinek, J. Guan et al., Hydrogen-catalyzed, pilot-scale production of small-diameter boron nitride nanotubes and their macroscopic assemblies. *ACS Nano* **8**, 6211–6220 (2014). <https://doi.org/10.1021/nn501661p>
17. A. Fathalizadeh, T. Pham, W. Mickelson, A. Zettl, Scaled synthesis of boron nitride nanotubes, nanoribbons, and nanococoons using direct feedstock injection into an extended-pressure, inductively-coupled thermal plasma. *Nano Lett.* **14**, 4881–4886 (2014). <https://doi.org/10.1021/nl5022915>
18. I. Narita, T. Oku, Synthesis of boron nitride nanotubes by using YB<sub>6</sub> powder. *Solid State Commun.* **122**, 465–468 (2002). [https://doi.org/10.1016/S0038-1098\(02\)00188-6](https://doi.org/10.1016/S0038-1098(02)00188-6)
19. J. Cumings, A. Zettl, Mass-production of boron nitride double-wall nanotubes and nanococoons. *Chem. Phys. Lett.* **316**, 211–216 (2000). [https://doi.org/10.1016/S0009-2614\(99\)01277-4](https://doi.org/10.1016/S0009-2614(99)01277-4)
20. Y. Chen, L.T. Chadderton, J.F. Gerald, J.S. Williams, A solid-state process for formation of boron nitride nanotubes. *Appl. Phys. Lett.* **74**, 2960–2962 (1999). <https://doi.org/10.1063/1.123979>
21. H. Chen, Y. Chen, Y. Liu, L. Fu, C. Huang et al., Over 1.0mm-long boron nitride nanotubes. *Chem. Phys. Lett.* **463**, 130–133 (2008). <https://doi.org/10.1016/j.cplett.2008.08.007>
22. D. Seo, J. Kim, S.-H. Park, Y.-U. Jeong, Y.-S. Seo et al., Synthesis of boron nitride nanotubes using thermal chemical vapor deposition of ball milled boron powder. *J. Ind. Eng. Chem.* **19**, 1117–1122 (2013). <https://doi.org/10.1016/j.jiec.2012.12.007>
23. D. Özmen, N.A. Sezgi, S. Balci, Synthesis of boron nitride nanotubes from ammonia and a powder mixture of boron and iron oxide. *Chem. Eng. J.* **219**, 28–36 (2013). <https://doi.org/10.1016/j.cej.2012.12.057>
24. L. Li, X. Liu, L. Li, Y. Chen, High yield BNNTs synthesis by promotion effect of milling-assisted precursor. *Microelectron. Eng.* **110**, 256–259 (2013). <https://doi.org/10.1016/j.mee.2013.01.044>
25. J.S. Maria Nithya, A., Pandurangan, Efficient mixed metal oxide routed synthesis of boron nitride nanotubes. *RSC Adv.* **4**, 26697–26705 (2014). <https://doi.org/10.1039/C4RA01204F>
26. P. Ahmad, M.U. Khandaker, Y.M. Amin, Synthesis of boron nitride nanotubes by Argon supported thermal chemical vapor deposition. *Phys. E Low Dimension. Syst. Nanostruct.* **67**, 33–37 (2015). <https://doi.org/10.1016/j.physe.2014.11.003>
27. L. Wang, T. Li, X. Long, X. Wang, Y. Xu et al., Bimetallic catalytic growth of boron nitride nanotubes. *Nanoscale* **9**, 1816–1819 (2017). <https://doi.org/10.1039/c6nr08623c>
28. E. Songfeng, C. Li, T. Li, R. Geng, Q. Li et al., Ammonium-tungstate-promoted growth of boron nitride nanotubes. *Nanotechnology* **29**, 195604 (2018). <https://doi.org/10.1088/1361-6528/aab12b>
29. L. Wang, D. Han, J. Luo, T. Li, Z. Lin et al., Highly efficient growth of boron nitride nanotubes and the thermal conductivity of their polymer composites. *J. Phys. Chem. C* **122**, 1867–1873 (2018). <https://doi.org/10.1021/acs.jpcc.7b10761>
30. C. Li, X. Long, E. Songfeng, Q. Zhang, T. Li et al., Magnesium-induced preparation of boron nitride nanotubes and their application in thermal interface materials. *Nanoscale* **11**, 11457–11463 (2019). <https://doi.org/10.1039/C9NR03915E>
31. D. Zhang, K. Zhang, E. Songfeng, D. Liu, C. Li et al., The MgB<sub>2</sub>-catalyzed growth of boron nitride nanotubes using B/MgO as a boron containing precursor. *Nanoscale Adv.* **2**, 2731–2737 (2020). <https://doi.org/10.1039/d0na00433b>
32. C.H. Lee, J. Wang, V.K. Kayatsha, J.Y. Huang, Y.K. Yap, Effective growth of boron nitride nanotubes by thermal chemical vapor deposition. *Nanotechnology* **19**, 455605 (2008). <https://doi.org/10.1088/0957-4484/19/45/455605>
33. A. Pakdel, C. Zhi, Y. Bando, T. Nakayama, D. Golberg, A comprehensive analysis of the CVD growth of boron nitride nanotubes. *Nanotechnology* **23**, 215601 (2012). <https://doi.org/10.1088/0957-4484/23/21/215601>

34. Y. Huang, Y. Bando, C. Tang, C. Zhi, T. Terao et al., Thin-walled boron nitride microtubes exhibiting intense band-edge UV emission at room temperature. *Nanotechnology* **20**, 085705 (2009). <https://doi.org/10.1088/0957-4484/20/8/085705>
35. A.T. Matveev, K.L. Firestein, A.E. Steinman, A.M. Kovalskii, I.V. Sukhorukova et al., Synthesis of boron nitride nanostructures from borates of alkali and alkaline earth metals. *J. Mater. Chem. A* **3**, 20749–20757 (2015). <https://doi.org/10.1039/C5TA05831G>
36. D. Köken, P. Sungur, H. Cebeci, F.Ç. Cebeci, Revealing the effect of sulfur compounds for low-temperature synthesis of boron nitride nanotubes from boron minerals. *ACS Appl. Nano Mater.* **5**, 2137–2146 (2022). <https://doi.org/10.1021/acsnm.1c03858>
37. S.-H. Chen, J. Su, Y. Wang, Y.-Q. Tang, X.-K. He, Thermodynamic assessment of  $B_2O_3$ – $MgO$  binary system. *Calphad* **51**, 67–74 (2015). <https://doi.org/10.1016/j.calphad.2015.07.004>
38. H.L. Li, R.Y.J. Tay, S.H. Tsang, L. Jing, M.M. Zhu et al., Composition-controlled synthesis and tunable optical properties of ternary boron carbonitride nanotubes. *RSC Adv.* **7**, 12511–12517 (2017). <https://doi.org/10.1039/C7RA00449D>
39. R.Y. Tay, H. Li, S.H. Tsang, L. Jing, D. Tan et al., Facile synthesis of millimeter-scale vertically aligned boron nitride nanotube forests by template-assisted chemical vapor deposition. *Chem. Mater.* **27**, 7156–7163 (2015). <https://doi.org/10.1021/acs.chemmater.5b03300>
40. L. Wu, B. Wang, Y. Zhang, L. Li, H.R. Wang et al., Structure and photoluminescence properties of a rare-earth free red-emitting  $Mn^{2+}$ -activated  $KMgBO_3$ . *Dalton Trans.* **43**, 13845–13851 (2014). <https://doi.org/10.1039/C4DT01524J>
41. J. Zheng, Q. Cheng, S. Wu, Y. Zhuang, Z. Guo et al., Structure, electronic properties, luminescence and chromaticity investigations of rare earth doped  $KMgBO_3$  phosphors. *Mater. Chem. Phys.* **165**, 168–176 (2015). <https://doi.org/10.1016/j.matchemphys.2015.09.012>
42. S.K.R.S. Sankaranarayanan, V.R. Bhethanabotla, B. Joseph, Molecular dynamics simulation study of the melting of Pd-Pt nanoclusters. *Phys. Rev. B* **71**, 195415 (2005). <https://doi.org/10.1103/physrevb.71.195415>
43. R. Subbaraman, S.K.R.S. Sankaranarayanan, Effect of Ag addition on the thermal characteristics and structural evolution of Ag-Cu-Ni ternary alloy nanoclusters: atomistic simulation study. *Phys. Rev. B* **84**, 075434 (2011). <https://doi.org/10.1103/physrevb.84.075434>
44. R. McCormack, F.D. De, First-principles study of multiple order-disorder transitions in  $Cd_2AgAu$  Heusler alloys. *Phys. Rev. B Condens. Matter* **54**, 9746–9755 (1996). <https://doi.org/10.1103/physrevb.54.9746>
45. L. Xie, P. Brault, A.-L. Thomann, J.-M. Bauchire,  $AlCoCrCuFeNi$  high entropy alloy cluster growth and annealing on silicon: a classical molecular dynamics simulation study. *Appl. Surf. Sci.* **285**, 810–816 (2013). <https://doi.org/10.1016/j.apsusc.2013.08.133>
46. S. Dehghani, Numerical study of long channel carbon nanotube based transistors by considering variation in CNT diameter. *J. Nano Res.* **61**, 78–87 (2020). <https://doi.org/10.4028/www.scientific.net/jnanor.61.78>
47. J.J. Fu, Y.N. Lu, H. Xu, K.F. Huo, X.Z. Wang et al., The synthesis of boron nitride nanotubes by an extended vapour–liquid–solid method. *Nanotechnology* **15**, 727–730 (2004). <https://doi.org/10.1088/0957-4484/15/7/003>
48. B. Santra, H.-Y. Ko, Y.-W. Yeh, F. Martelli, I. Kaganovich et al., Root-growth of boron nitride nanotubes: experiments and *ab initio* simulations. *Nanoscale* **10**, 22223–22230 (2018). <https://doi.org/10.1039/C8NR06217J>
49. B. McLean, G.B. Webber, A.J. Page, Boron nitride nanotube nucleation via network fusion during catalytic chemical vapor deposition. *J. Am. Chem. Soc.* **141**, 13385–13393 (2019). <https://doi.org/10.1021/jacs.9b03484>
50. N. Wang, L. Ding, T. Li, K. Zhang, L. Wu et al., Self-catalytic ternary compounds for efficient synthesis of high-quality boron nitride nanotubes. *Small* **19**, e2206933 (2023). <https://doi.org/10.1002/sml.202206933>
51. A.B. Meshalkin, A.B. Kaplun, The complex investigation of the phase equilibria and melt characteristics in borate and silicate systems. *J. Cryst. Growth* **275**, e115–e119 (2005). <https://doi.org/10.1016/j.jcrysgro.2004.10.136>
52. S.M. Howard, Ellingham diagrams, SD School of Mines and Technology, Rapid City, SD, **2006**
53. L. Wu, Y. Bai, L. Wu, H. Yi, X. Zhang et al., Analysis of the structure and abnormal photoluminescence of a red-emitting  $LiMgBO_3: Mn^{2+}$  phosphor. *Dalton Trans.* **47**, 13094–13105 (2018). <https://doi.org/10.1039/C8DT02450B>
54. J. Zhong, Y. Zhuo, S. Hariyani, W. Zhao, J. Wen et al., Closing the cyan gap toward full-spectrum LED lighting with  $NaMgBO_3: Ce^{3+}$ . *Chem. Mater.* **32**, 882–888 (2020). <https://doi.org/10.1021/acs.chemmater.9b04739>
55. Z. Wang, M. Zhang, S. Pan, Z. Yang, H. Zhang et al., Exploring the influence of cationic skeletons on the arrangement of isolated  $BO_3$  groups based on  $RbMgBO_3$ ,  $CsZn_4(BO_3)_3$  and  $Cs_4Mg_4(BO_3)_4$ . *New J. Chem.* **38**, 3035–3041 (2014). <https://doi.org/10.1039/C4NJ00363B>
56. Y. Zhu, X. Shen, D. Bao, Y. Shi, H. Huang et al., Nano SiC enhancement in the BN micro structure for high thermal conductivity epoxy composite. *J. Polym. Res.* **28**, 387 (2021). <https://doi.org/10.1007/s10965-021-02755-z>

**Publisher's note** Springer Nature remains neutral with regard to jurisdictional claims in published maps and institutional affiliations.

